Parallel p—n Junctions across Nanowires by One-Step *Ex Situ* Doping

Ori Hazut,[†] Bo-Chao Huang,[‡] Adi Pantzer,[§] Iddo Amit,[⊥] Yossi Rosenwaks,[⊥] Amit Kohn,[§] Chia-Seng Chang,[∥] Ya-Ping Chiu,[‡,*] and Roie Yerushalmi[†,*]

[†]Institute of Chemistry and the Center for Nanoscience and Nanotechnology, The Hebrew University of Jerusalem, Edmond J. Safra Campus, Givat Ram, Jerusalem 91904, Israel, [‡]Department of Physics, National Sun Yat-sen University, Kaohsiung 80424, Taiwan, [§]Department of Materials Engineering and the Ilse Katz Institute for Nanoscale Science and Technology, Ben-Gurion University of the Negev, Beer-Sheva 8410501, Israel, [⊥]Department of Physical Electronics, School of Electrical Engineering, Tel-Aviv University, Tel-Aviv 69978, Israel, and [∥]Institute of Physics, Academia Sinica, Nankang, Taipei 115, Taiwan

ABSTRACT The bottom-up synthesis of nanoscale building blocks is a versatile approach for the formation of a vast array of materials with controlled structures and compositions. This approach is one of the main driving forces for the immense progress in materials science and nanotechnology witnessed over the past few decades. Despite the overwhelming advances in the bottom-up synthesis of nanoscale building blocks and the fine control of accessible compositions and structures, certain aspects are still lacking. In particular, the transformation of symmetric nanostructures to asymmetric nanostructures by highly controlled processes while preserving the modified structural orientation still poses a significant challenge. We present a one-step *ex situ* doping process for the transformation of undoped silicon nanowires (i-Si NWs) to p-type/n-type (p—n) parallel p—n junction configuration across NWs. The vertical p—n junctions were measured by scanning tunneling microscopy (STM) in concert with scanning tunneling spectroscopy (STS), termed STM/S, to obtain the spatial electronic properties of the junction formed across the NWs. Additionally, the parallel p—n junction configuration was characterized by off-axis electron holography in a transmission electron microscope to provide an independent verification of junction formation. The doping process was simulated to elucidate the doping mechanisms involved in the one-step p—i—n junction formation.

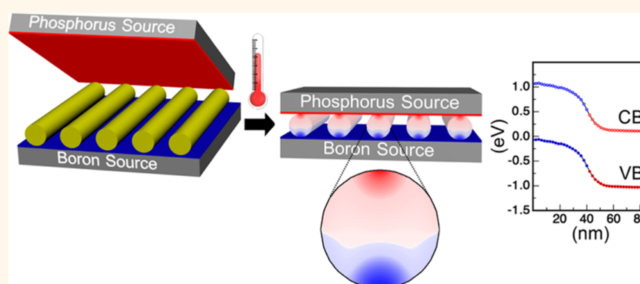

KEYWORDS: nanowires · doping · silicon · monolayer doping · surface chemistry

Control of the electronic properties of semiconductors (SCs) is achieved primarily by the incorporation of impurity atoms, termed dopants, which alter the semiconductor's electronic structure and properties by creating excess electrons (*n-type*) or holes (*p-type*) in the SC. The controlled doping of SCs is the basis of microelectronics,[1,2] photovoltaics,[3] semiconductor lasers,[4] and nanowire (NW) devices and sensors.[5,6] Although advanced methodologies for the controlled doping of top-down fabricated SC structures have become available in recent years and remarkable advances have been made in this field, the controlled doping of nanoscale structures still poses significant challenges.[7−16] The continuous endeavor to achieve the controlled doping of SC structures with smaller dimensions poses significant challenges in the semiconductor industry and at the frontiers of material science. Thus, achieving highly controlled dopant distribution and positioning in nanostructures is highly attractive and expected to provide significant new capabilities.

To this end, we present a one-step method for transforming undoped silicon NWs (i-Si NWs) into nanoscale building blocks featuring parallel p—i—n junctions with well-controlled dopant distributions. Different aspects of nanoscale registry are the topic of ongoing research.[17−19] Specifically, orientation registry at the nanoscale is a desirable property for enabling the further analysis and processing of nanoscale structures. The simple method presented herein yields both controlled dopant distribution within the nanoscale structure and the deterministic orientation of the resulting asymmetric structure relative to the macroscopic framework.

The parallel p—n junctions are formed by a one-step process that is applied to i-Si NW

* Address correspondence to roie.yerushalmi@mail.huji.ac.il, ypchiu@mail.nsysu.edu.tw.

Received for review May 26, 2014 and accepted July 16, 2014.

Published online July 16, 2014
10.1021/nn502855k

© 2014 American Chemical Society

ARTICLE

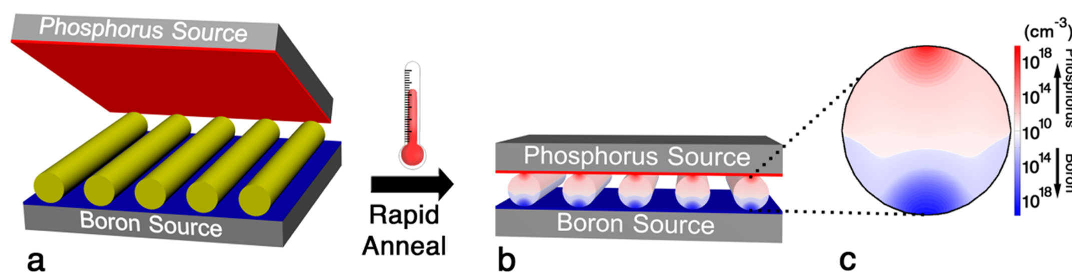

Figure 1. Schematic of parallel p−n junction configuration formation across oriented NWs by a one-step contact doping process. (a) Intrinsic Si NWs are transferred to a pretreated substrate with a monolayer containing boron functionalities and then covered by a second pretreated substrate with a phosphorus-containing monolayer. (b) Sample is annealed by rapid thermal anneal (RTA) in a vacuum, which results in the controlled decomposition of the monolayers and dopant diffusion onto the NWs. (c) Process yields parallel p−n junction configuration NWs.

arrays (Figure 1). The doping process relies on a monolayer contact doping (MLCD) technique, which utilizes monolayers as a source for dopant atoms.[15,20] The MLCD process was previously demonstrated to deliver highly controlled formation of doping profiles for Si, with steep dopant concentration profiles spanning several orders of magnitude from the modified interface into the bulk.[15,16]

RESULTS AND DISCUSSION

The parallel p−n junctions were measured by scanning tunneling microscopy (STM) in concert with scanning tunneling spectroscopy (STS), termed STM/S, to obtain the spatial electronic properties of the junction formed across the NWs. Additionally, the built-in potentials in the parallel p−n junctions were also measured by off-axis electron holography (OAEH) in a transmission electron microscope to provide an independent verification of junction formation. To directly investigate the characteristics of the parallel p−n junction formed by the one-step process, the sample was transferred to an ultrahigh vacuum chamber under a background pressure of less than 1×10^{-10} Torr and cleaved *in situ* (Supporting Information Figure S2). Cross-sectional scanning tunneling microscopy (XSTM) was applied to the *in situ*-cleaved NW samples, avoiding possible surface contamination and revealing the correlation between the nanoscale morphology and *local* electronic structure through the *cross-sectional* profile of the NW. The STM and STS images were simultaneously acquired at approximately 100 K. The topographic imaging was conducted at a constant current of 0.4 nA and at a sample voltage of −3 V. The tunneling spectra were acquired by utilizing the current imaging tunneling spectroscopy mode, in which a series of tunneling current images were obtained at different sample bias voltages, V_s. In this research, V_s was varied from +4.0 to −4.0 V for STS measurements. Representative STM images and cross-sectional analyses of a Si NW are presented in Figure 2. The STM/S results demonstrate the formation of parallel p−n junctions across the Si NW by the one-step *ex situ* doping process presented in Figure 1. Supporting Information Figure S3 presents further structural analyses of the NW cross section.

The Si doped with B and P resulted in p- and n-type electronic characteristics, respectively, as evidenced by the shift in the conduction band edge relative to the Fermi level (Figure 2f). The two-dimensional (2D) cross-sectional spatial dependence of the density of states, measured at −3.5 V, for the parallel junction configuration doped Si NW is presented in Figure 2b. Additionally, the variations of the d*I*/d*V* signal within the doped NW were imaged (Supporting Information Figure S4). The STM/S spectroscopic data provide quantitative mapping of dopant distributions, electrostatic potential, and local band structures within the doped NWs (Figure 2c,e,f, respectively). See the Supporting Information for further details of the dopant concentration analysis and related properties from the spectroscopic data (Supporting Information Figures S5 and S6). Special care was taken in considering the tip-induced band bending effect for the STM measurements by performing three-dimensional (3-D) potential calculations for a STM tip near a semiconductor surface (see Supporting Information Figures S7−S12 and additional details in the Supporting Information).[21,22] The high-resolution, quantitative, STM/S 2D mapping of dopant distributions across the parallel NW junction provides valuable insights into the details of the underlying doping mechanism. Our data demonstrate that the parallel p−n junction follows the expected polarity imposed by the macroscopic process depicted in Figure 1, with the p- and n-type regions at the respective poles of the NW in accordance with the B and P dopant source positions utilized in the one-step process. The dopant surface concentration at the P-doped pole was 2.6×10^{19} cm^{-3}, whereas that at the B-doped pole was 1.0×10^{20} cm^{-3}. The doping concentration at the NW core was 3 orders of magnitude smaller, exhibiting a compensated region with approximately 10^{17} cm^{-3} n- and p-type dopant concentrations at the respective NW core regions. Overall, the one-step NW doping process yielded parallel n^{-}−i−p^{+} junctions across the NWs. Specifically, the n-type dopant distribution exhibited a diffusion profile with

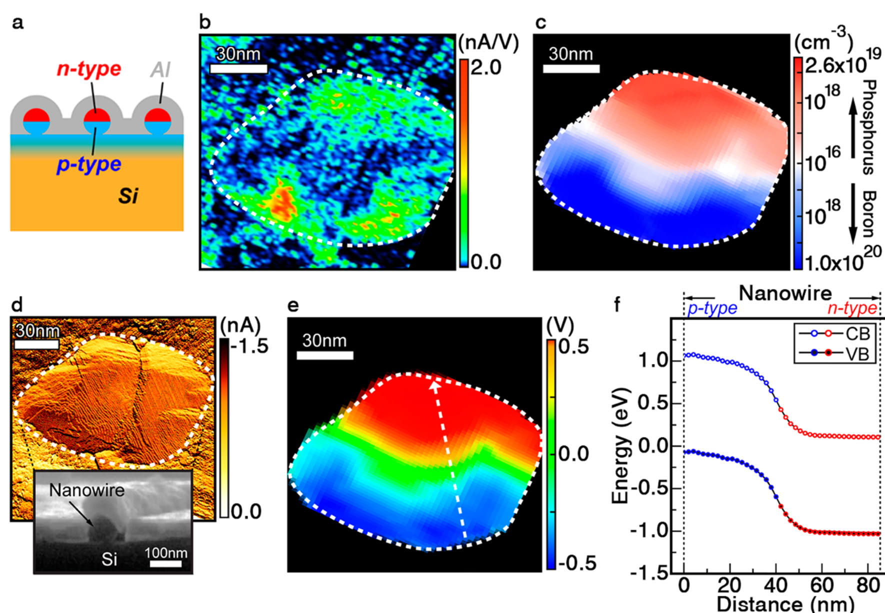

Figure 2. Cross-sectional STM/S analysis of *ex situ*-doped Si NWs. (a) Schematic of the parallel NW junction configuration (cross-sectional view). (b) STM/S spectroscopic d*I*/d*V* image recorded at −3.5 V sample bias and (c) dopant concentration distribution across the NW junction. (d) Typical cross-sectional STM image of the NW obtained at a sample bias of −3.0 V. Inset: SEM secondary electron image displaying the geometrical structure of the NW from the cross-sectional view. (e) Electrostatic potential distribution mapping, obtained by analyzing the STM/S data, that demonstrates the formation of a junction in the NW. (f) Conduction band edge and valence band edge switched from p- to n-type across the NW, corresponding to the B- and P-doped poles, respectively, along the dashed arrow trajectory in (e). The white dashed oval curve outlines the NW boundary.

a maximal dopant concentration at the NW surface contact region, with a monotonic decrease in dopant concentration away from the NW surface and toward the core that is consistent with limited source doping, as provided by the monolayer in contact with the NW's surface.[15] For the p-type-doped region corresponding to Si doped with B atoms, in addition to the high doping levels that extended from the NW surface contact region, we also observed high levels of dopants at the NW's surface semicircumference that decreased toward the NW core. Experimentally, from our STM measurements, the conduction band minimum changed by approximately 1.0 eV (the junction's built-in potential) from the n- to p-type poles of the NW's parallel junction configuration. An additional independent verification and characterization of the parallel p−n junction configuration formed across the Si NWs was achieved by OAEH. OAEH maps the electrostatic potential at a spatial resolution of approximately 5 nm by determining the mean inner potential of the sample from the reconstructed phase of the electron wave.[23−27] These measurements were performed on thin lamellar cross-sectional slices of the doped NWs and were compared to those of undoped, intrinsic NWs (see Supporting Information Figures S13−S17 and additional details concerning the measurements and methodology in the Supporting Information). The OAEH measurements indicated a built-in potential difference of 1.0 ± 0.2 V along the direction of the doped NWs, whereas in the perpendicular direction, the potential differences were within the 0.2 V sensitivity of this technique.

A comparable OAEH measurement of an intrinsic NW exhibited an approximately constant electrostatic potential throughout the NW, within the 0.2 V accuracy of this method (Supporting Information Figures S18−S20).

Two doping mechanisms were considered and simulated to account for the junction characteristics measured by the STM/S and OAEH. The first mechanism is termed contact doping (CD), which was previously introduced and studied by our group,[15] and the second mechanism is termed proximity doping (PD) (Figure 3a−c). In the CD mechanism (Figure 3a), dopant atoms diffuse exclusively between the donor substrate and NW in the donor substrate−NW contact region. The PD mechanism (Figure 3b) involves the evaporation of fragments originating from the thermally decomposed monolayer containing dopant atoms. Monolayer decomposition and fragment evaporation occurs *in situ* during the rapid thermal anneal process at high-temperature (970 °C) and vacuum (10^{-2} Torr) conditions during the processing. The contribution of the PD mechanism to the total dopant concentration depends on the mean free path at the specific processing temperature and pressure conditions and on the surface interactions between the monolayer fragments and surface oxide, including surface diffusion and covalent and noncovalent interactions, which vary for the different surface chemistries and thermal degradation processes of the P and B

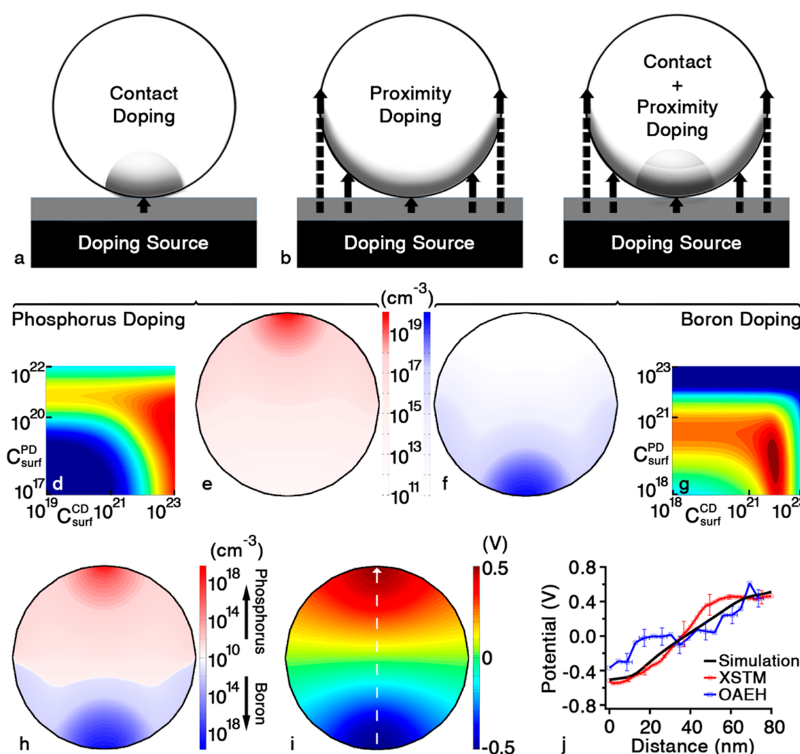

Figure 3. Mechanisms of dopant incorporation and distribution in the formation of a parallel p−n junction configuration across NWs. (a−c) Suggested dopant distribution mechanism. (a) Diffusion of dopants through the oxide contact regions, termed CD. (b) During the thermal decomposition of the monolayers, the evaporation of fragments onto the NW surface results in PD. (c) Suggested doping mechanism involves contributions from both CD and PD. Process simulation of dopant incorporation and distribution in the formation of a parallel p−n junction configuration across NW (d−g). Simulated dopant distribution maps obtained for P (e) and B (f) with CD and PD contributions. The contributions of the CD and PD mechanisms were determined by a global best-fit optimization comparing the simulated processes to the total dopant distribution maps obtained by the STM/S measured data and are presented in (d) and (g) for P and B, respectively. (h) Simulated compensated dopant map, (i) corresponding 2D electrostatic potential map, and (j) potential along the dashed arrow trajectory shown in (i) from p- to n-type for the simulated NW junction, as measured by XSTM and OAEH. All process simulations were performed for intrinsic NWs (80 nm diameter) at equivalent conditions, as further described in the Supporting Information.

monolayers.[15,28] The two doping mechanisms, CD and PD, were simulated for B and P dopant atoms using the Sentaurus technology computer-aided design (TCAD) process simulator (Synopsys Inc. Mountain View, CA, USA) to quantify the contribution of the respective doping mechanisms involved in the one-step p−i−n junction formation to understand the overall process. Briefly, CD and PD were simulated by two types of processes modeled with characteristic initial conditions for the dopant source distribution, followed by diffusion simulation. The CD process was simulated by modeling a uniform distribution of dopants with surface concentration C^{CD}_{Surf} placed at the planar oxide substrate in contact with the NW surface and simulated thermal anneal. The PD process was simulated by modeling the evaporation of an oxide layer containing dopants at a specified concentration C^{PD}_{Surf} onto the NW semicircumference facing the planar oxide substrate and simulated thermal anneal (see Supporting Information Figure S1 and additional simulation details). The diffusion simulations were performed following the actual temperature profiles measured during the experimental RTA process (Supporting Information Figure S1c). The 2D dopant distribution maps were obtained by process simulations for a range of initial surface concentrations C^{CD}_{Surf} and C^{PD}_{Surf} for both P and B. The dopant distributions obtained by the simulations were compared to the measured STM/S 2D dopant distribution, yielding a best-fit map for each dopant type and the respective contributions of the CD and PD to the overall process (Figure 3d−g). The measured dopant distribution maps generated by STM/S could be reproduced by a combination of simulated CD and PD doping schemes. For both P and B, the best fit between the STM/S 2D-measured dopant distribution and simulated dopant distribution corresponds to a predominantly CD-based doping mechanism with an additional lesser contribution of PD (Figure 3d,g). Although the contribution of the PD mechanism was less than 1% for both P and B, as quantified by the ratio $C^{PD}_{Surf}/C^{CD}_{Surf}$, we found that the inclusion of the PD mechanism was required to correctly reproduce the measured 2D dopant map. The best-fit dopant profiles obtained by the combined CD and PD simulations for P and B were used to calculate the total dopant distribution maps (compensated dopant distribution,

Figure 3h) and to derive the corresponding 2D electrostatic potential map (Figure 3i). We obtained good agreement between the experimental and simulated results, including the dopant distribution maps, electrostatic potential, and conduction and valence band shifts along the parallel p−i−n junction. Note that under the experimental conditions employed in our study for measuring d*I*/d*V* spectra, the detection limit for dopant concentrations is $\sim 10^{16}$ cm^{-3} In contrast, the simulations do not have this technical limitation and therefore show significantly lower doping levels at the core region. The three methodologies used, STM/S, OAEH, and the simulated process and computational analysis, were in close agreement, yielding a 1.0 V potential difference across the *ex situ*-doped parallel p−i−n junction (Figure 3j). Local variations as a result of NW diameter distribution may result in variations in the contribution of CD mechanism relative to PD. Systematic study of the contribution of PD to the overall doping process is currently under further study.

CONCLUSIONS

The presented postgrowth, *ex situ* doping methodology provides a high level of control over dopant distribution at the nanoscale level with concomitant preservation of the resultant asymmetric structure orientation that is critical for utilizing nanoscale building blocks for different applications. The method utilizes tailored surface chemistry optimized for B and P doping of Si. Resolving the contributions of the two types of doping mechanisms taking place in tandem during the rapid thermal anneal process provided insight for achieving the demonstrated level of process controllability. The combination of bottom-up synthesis of nanoscale building blocks with postgrowth, *ex situ* doping methodology benefits from the vast range of structures and compositions attainable by the former with the high level of control and registry offered by the latter leading to new structures with tailored electronic properties.

METHODS

Monolayer Formation. Si wafers were cleaned by submersion in an acid piranha solution (3:1 mixture of concentrated sulfuric acid to 30% hydrogen peroxide) for 15 min, followed by dipping in a base piranha solution (5:1:1 mixture of deionized water to 25% ammonium hydroxide to 30% hydrogen peroxide) for 8 min at 60 °C in a sonication bath. The P donor substrates were prepared by reacting the freshly cleaned Si wafers in mesitylene solution containing 40 mM tetraethyl methylenediphosphonate for 2 h at 100 °C, followed by rinsing in mesitylene and dichloromethane. Similarly, the B donor substrates were prepared by reacting freshly cleaned wafers in a 35 mM solution of phenylboronic acid in mesitylene for 2 h at 100 °C, followed by rinsing in mesitylene and dichloromethane.

Caution: Piranha solutions are extremely strong and dangerous oxidizing agents and should be used with extreme caution. May explode in contact with organic solvents.

Preparation of Si NWs. The Si NWs were synthesized by cleaning glass slides under 60 W O_2 plasma for 2 min. Then, a poly-L-lysine solution was applied to the glass surface, and the slides were rinsed with deionized water for 5 min. An 80 nm gold colloid solution was applied to the glass surface for 2 min and then removed by rinsing with deionized water. The NWs were grown in a chemical vapor deposition system at 440 °C and 35 Torr under a flow of SiH_4 (2 sccm) and H_2 (50 sccm) for 30 min.

Doping of Si NWs. The Si NWs were transferred to a phenylboronic acid-reacted Si/SiO_2 substrate by contact printing,[29] covered with the tetraethyl methylenediphosphonate-reacted Si/SiO_2 substrate, and annealed at 970 °C for 20 s using an AnnealSYS MicroAS system. Prior to the annealing step, the chamber was purged with Ar and then evacuated to a pressure of 10−2 Torr. The heating was carried out at 160 °C/s. A blank process before each MLCD process was applied to remove residual dopants from the chamber.

Conflict of Interest: The authors declare no competing financial interest.

Acknowledgment. This work was supported in part by the a starting grant from the European Research Council (ERC) under the European Community's Seventh Framework Programme Grant Agreement No. 259312, and the United States−Israel Binational Science Foundation.

Supporting Information Available: Detailed sample preparation procedures, instrument specifications, analysis of electron images microscopy (STM, STS, electron holography, TEM, HRTEM, and SEM), and dopant diffusion simulations. This material is available free of charge *via* the Internet at http://pubs.acs.org.

REFERENCES AND NOTES

1. Thelander, C.; Agarwal, P.; Brongersma, S.; Eymery, J.; Feiner, L. F.; Forchel, A.; Scheffler, M.; Riess, W.; Ohlsson, B. J.; Gosele, U.; *et al.* Nanowire-Based One-Dimensional Electronics. *Mater. Today* **2006**, *9*, 28–35.
2. Gandhi, R.; Chen, Z. X.; Singh, N.; Banerjee, K.; Lee, S. CMOS-Compatible Vertical-Silicon-Nanowire Gate-All-Around p-Type Tunneling FETs with ≤ 50-mV/decade Subthreshold Swing. *IEEE Electron Device Lett.* **2011**, *32*, 1504–1506.
3. Czaban, J. A.; Thompson, D. A.; LaPierre, R. R. GaAs Core−Shell Nanowires for Photovoltaic Applications. *Nano Lett.* **2009**, *9*, 148–154.
4. Yang, C.; Zhong, Z. H.; Lieber, C. M. Encoding Electronic Properties by Synthesis of Axial Modulation-Doped Silicon Nanowires. *Science* **2005**, *310*, 1304–1307.
5. Patolsky, F.; Zheng, G. F.; Hayden, O.; Lakadamyali, M.; Zhuang, X. W.; Lieber, C. M. Electrical Detection of Single Viruses. *Proc. Natl. Acad. Sci. U.S.A* **2004**, *101*, 14017–14022.
6. Garnett, E. C.; Brongersma, M. L.; Cui, Y.; McGehee, M. D. Nanowire Solar Cells. *Annu. Rev. Mater. Res.* **2001**, *41*, 269–295.
7. Kempa, T. J.; Tian, B. Z.; Kim, D. R.; Hu, J. S.; Zheng, X. L.; Lieber, C. M. Single and Tandem Axial p−i−n Nanowire Photovoltaic Devices. *Nano Lett.* **2008**, *8*, 3456–3460.
8. Tian, B. Z.; Zheng, X. L.; Kempa, T. J.; Fang, Y.; Yu, N. F.; Yu, G. H.; Huang, J. L.; Lieber, C. M. Coaxial Silicon Nanowires as Solar Cells and Nanoelectronic Power Sources. *Nature* **2007**, *449*, 885–889.
9. Amit, I.; Givan, U.; Connell, J. G.; Paul, D. F.; Hammond, J. S.; Lauhon, L. J.; Rosenwaks, Y. Spatially Resolved Correlation of Active and Total Doping Concentrations in VLS Grown Nanowires. *Nano Lett.* **2013**, *13*, 2598–2604.
10. Koren, E.; Hyun, J. K.; Givan, U.; Hemesath, E. R.; Lauhon, L. J.; Rosenwaks, Y. Obtaining Uniform Dopant Distributions in VLS-Grown Si Nanowires. *Nano Lett.* **2011**, *11*, 183–187.
11. Misra, N.; Grigoropoulos, C. P.; Stumbo, D. P.; Miller, J. N. Laser Activation of Dopants for Nanowire Devices on Glass and Plastic. *Appl. Phys. Lett.* **2008**, *93*, 121116.

12. Wallentin, J.; Borgstrom, M. T. Doping of Semiconductor Nanowires. *J. Mater. Res.* **2011**, *26*, 2142–2156.
13. Murthy, D. H. K.; Xu, T.; Chen, W. H.; Houtepen, A. J.; Savenije, T. J.; Siebbeles, L. D. A.; Nys, J. P.; Krzeminski, C.; Grandidier, B.; Stievenard, D.; *et al.* Efficient Photogeneration of Charge Carriers in Silicon Nanowires with a Radial Doping Gradient. *Nanotechnology* **2011**, *22*, 315710.
14. Yoo, J.; Dayeh, S. A.; Tang, W.; Picraux, S. T. Epitaxial Growth of Radial Si p−i−n Junctions for Photovoltaic Applications. *Appl. Phys. Lett.* **2013**, *102*, 093113.
15. Hazut, O.; Agarwala, A.; Amit, I.; Subramani, T.; Zaidiner, S.; Rosenwaks, Y.; Yerushalmi, R. Contact Doping of Silicon Wafers and Nanostructures with Phosphine Oxide Monolayers. *ACS Nano* **2012**, *6*, 10311–10318.
16. Ho, J. C.; Yerushalmi, R.; Jacobson, Z. A.; Fan, Z.; Alley, R. L.; Javey, A. Controlled Nanoscale Doping of Semiconductors *via* Molecular Monolayers. *Nat. Mater.* **2008**, *7*, 62–67.
17. Jin, S.; Whang, D. M.; McAlpine, M. C.; Friedman, R. S.; Wu, Y.; Lieber, C. M. Scalable Interconnection and Integration of Nanowire Devices without Registration. *Nano Lett.* **2004**, *4*, 915–919.
18. Daoulas, K. C.; Muller, M.; Stoykovich, M. P.; Park, S. M.; Papakonstantopoulos, Y. J.; de Pablo, J. J.; Nealey, P. F.; Solak, H. H. Fabrication of Complex Three-Dimensional Nanostructures from Self-Assembling Block Copolymer Materials on Two-Dimensional Chemically Patterned Templates with Mismatched Symmetry. *Phys. Rev. Lett.* **2006**, *96*, 036104.
19. Cheng, J. Y.; Ross, C. A.; Smith, H. I.; Thomas, E. L. Templated Self-Assembly of Block Copolymers: Top-Down Helps Bottom-Up. *Adv. Mater.* **2006**, *18*, 2505–2521.
20. Hazut, O.; Agarwala, A.; Subramani, T.; Waichman, S.; Yerushalmi, R. Monolayer Contact Doping of Silicon Surfaces and Nanowires Using Organophosphorus Compounds. *J. Vis. Exp.* **2013**, *82*, e50770.
21. Feenstra, R. M. Electrostatic Potential for a Hyperbolic Probe Tip near a Semiconductor. *J. Vac. Sci. Technol., B* **2003**, *21*, 2080–2088.
22. Ishida, N.; Sueoka, K.; Feenstra, R. M. Influence of Surface States on Tunneling Spectra of n-Type GaAs(110) surfaces. *Phys. Rev. B* **2009**, *80*, 075320.
23. McCartney, M. R.; Agarwal, N.; Chung, S.; Cullen, D. A.; Han, M. G.; He, K.; Li, L. Y.; Wang, H.; Zhou, L.; Smith, D. J. Quantitative Phase Imaging of Nanoscale Electrostatic and Magnetic Fields Using Off-Axis Electron Holography. *Ultramicroscopy* **2010**, *110*, 375–382.
24. Lichte, H.; Formanek, P.; Lenk, A.; Linck, M.; Matzeck, C.; Lehmann, M.; Simon, P. Electron Holography: Applications to Materials Questions. *Annu. Rev. Mater. Res.* **2007**, *37*, 539–588.
25. Gan, Z. F.; Perea, D. E.; Yoo, J.; Picraux, S. T.; Smith, D. J.; McCartney, M. R. Mapping Electrostatic Profiles Across Axial p−n Junctions in Si Nanowires Using Off-Axis Electron Holography. *Appl. Phys. Lett.* **2013**, *103*, 153108.
26. He, K.; Cho, J. H.; Jung, Y.; Picraux, S. T.; Cumings, J. Silicon Nanowires: Electron Holography Studies of Doped p−n Junctions and Biased Schottky Barriers. *Nanotechnology* **2013**, *24*, 115703.
27. den Hertog, M. I.; Schmid, H.; Cooper, D.; Rouviere, J. L.; Bjork, M. T.; Riel, H.; Rivallin, P.; Karg, S.; Riess, W. Mapping Active Dopants in Single Silicon Nanowires Using Off-Axis Electron Holography. *Nano Lett.* **2009**, *9*, 3837–3843.
28. Agarwala, A.; Subramani, T.; Goldbourt, A.; Danovich, D.; Yerushalmi, R. Facile Monolayer Formation on SiO_2 Surfaces *via* Organoboron Functionalities. *Angew. Chem., Int. Ed.* **2013**, *52*, 7415–7418.
29. Fan, Z. Y.; Ho, J. C.; Jacobson, Z. A.; Yerushalmi, R.; Alley, R. L.; Razavi, H.; Javey, A. Wafer-Scale Assembly of Highly Ordered Semiconductor Nanowire Arrays by Contact Printing. *Nano Lett.* **2008**, *8*, 20–25.